Sawazaki et al. Progress in Earth and Planetary Science (2016) 3:36
DOI 10.1186/s40645-016-0112-7

Progress in Earth and Planetary Science

RESEARCH ARTICLE Open Access

Estimation of seismic velocity changes at different depths associated with the 2014 Northern Nagano Prefecture earthquake, Japan (M_W 6.2) by joint interferometric analysis of NIED Hi-net and KiK-net records

Kaoru Sawazaki*, Tatsuhiko Saito, Tomotake Ueno and Katsuhiko Shiomi

Abstract

To estimate the seismic velocity changes at different depths associated with a large earthquake, we apply passive image interferometry to two types of seismograms: KiK-net vertical pairs of earthquake records and Hi-net continuous borehole data. We compute the surface/borehole deconvolution waveform (DCW) of seismograms recorded by a KiK-net station and the autocorrelation function (ACF) of ambient noise recorded by a collocated Hi-net station, 26 km from the epicenter of the 2014 Northern Nagano Prefecture earthquake, Japan (M_W 6.2). Because the deeper KiK-net sensor and the Hi-net sensor are collocated at 150 m depth, and another KiK-net sensor is located at the surface directly above the borehole sensors, we can measure shallow (<150 m depth) and deep (>150 m depth) velocity changes separately. The sensitivity of the ACF to the velocity changes in the deeper zone is evaluated by a numerical wave propagation simulation. We detect relative velocity changes of −3.1 and −1.4% in the shallow and deep zones, respectively, within 1 week of the mainshock. The relative velocity changes recover to −1.9 and −1.1%, respectively, during the period between 1 week and 4 months after the mainshock. The observed relative velocity reductions can be attributed to dynamic strain changes due to the strong ground motion, rather than static strain changes due to coseismic deformation by the mainshock. The speed of velocity recovery may be faster in the shallow zone than in the deep zone because the recovery speed is controlled by initial damage in the medium. This recovery feature is analogous to the behavior of slow dynamics observed in rock experiments.

Keywords: Time-lapse monitoring, Velocity change and recovery, Passive image interferometry, Wave propagation simulation, Dynamic and static strain changes, Slow dynamics

Introduction

Even though seismic velocity changes associated with large earthquakes have been widely studied for decades (e.g., Poupinet et al. 1984), the cause of the observed velocity changes is still debated. Seismic motion is significantly amplified in low-velocity sediments and sometimes induces severe damage to the shallow subsurface (e.g., Rubinstein and Beroza 2005; Sawazaki et al. 2009). On the other hand, static crustal deformation associated with a large earthquake also induces damage to the subsurface medium, in particular near the earthquake fault (e.g., Brenguier et al. 2008). Both dynamic (strong ground motion) and static (crustal deformation) strain changes are the possible causes of observed seismic velocity changes. However, it is difficult to evaluate the contribution of each factor to seismic velocity changes because the spatial resolutions of the velocity changes associated with these phenomena are poorly understood.

To detect shallow velocity changes separately from changes at greater depths, previous studies used pairs of seismograms from vertically offset instruments, e.g., paired sensors in a single vertical borehole (e.g.,

* Correspondence: sawa@bosai.go.jp
National Research Institute for Earth Science and Disaster Resilience, Tsukuba, Japan

Sawazaki et al. 2009; Nakata and Snieder 2012; Takagi et al. 2012). According to these studies, velocity reduction is concentrated in the topmost layers (generally shallower than several hundred meters) because the layers are severely damaged by strong ground motion. On the other hand, some studies have detected velocity changes associated with earthquake swarms (e.g., Maeda et al. 2010; Ueno et al. 2012), postseismic deformation (e.g., Brenguier et al. 2008), and slow slip (e.g., Rivet et al. 2011), which are not accompanied by strong ground motion. This suggests that both dynamic and static strain changes are likely to cause velocity changes and that their relative contributions may change with depth.

The sensitivity of the seismic wavefield can also be used to estimate velocity changes in shallow and deep zones separately. Hobiger et al. (2012) analyzed the different frequency ranges of the cross-correlation functions of ambient noise records and reported that velocity reduction due to a large earthquake is larger at higher frequencies. Because surface waves are more sensitive to shallow structure at high frequencies, this result suggests that velocity reduction is more significant at shallower depths. Recently, the sensitivity kernel of the seismic wavefield, reconstructed by analytical (e.g., Pacheco and Snieder 2005, 2006) and numerical (e.g., Obermann et al. 2013a; Kanu and Snieder 2015) approaches, has been used in an inversion scheme that can resolve spatial variations in velocity changes (e.g., Obermann et al. 2013b). A more direct approach that uses the sensitivity of the phase delay curves to partial velocity changes has been developed to investigate spatial variations (e.g., Yang et al. 2014; Sawazaki et al. 2015). However, because the accuracy of the sensitivity kernel strongly depends on the short-wavelength velocity structure, which is not sufficiently determined in most areas, the utility of the sensitivity kernel is still limited, especially with respect to depth resolution.

To further investigate the seismic velocity changes associated with large earthquakes at different depths, vertical pairs of seismograms and sensitivity of the seismic wavefield should be used in combination. In this study, we apply the passive image interferometry technique (e.g., Sens-Schönfelder and Wegler 2006) to two different types of collocated seismometers. The first is a vertical pair of strong motion accelerometers from KiK-net, installed at the surface and the bottom of a borehole (150 m deep). The second is a Hi-net high-sensitivity seismometer collocated with the KiK-net borehole bottom accelerometer (Fig. 1b). Both seismograph networks are operated by the National Research Institute for Earth Science and Disaster Resilience (NIED) of Japan (Okada et al. 2004). The surface/borehole deconvolution waveform (DCW) of the KiK-net seismograms is suitable to reconstruct the transfer function from 150 m depth to the surface (Snieder and Şafak 2006). Hi-net continuous records are suitable for reconstructing the autocorrelation function (ACF) of the ambient noise (e.g., Ueno et al. 2015), which approximately represents the zero-offset Green's function (Claerbout 1968). The retrieved DCW is sensitive to changes in the medium above 150 m depth, while the ACF is sensitive to changes in the medium both above and below 150 m. To evaluate the sensitivity of the ACF to the partial velocity changes above and below the 150 m depth cutoff, we perform a numerical wave propagation simulation based on a realistic velocity model. We then independently estimate the velocity changes above and below the 150 m depth cutoff associated with the M_W 6.2 Northern Nagano Prefecture earthquake, Japan (hereafter referenced as the "N. Nagano earthquake"), which occurred on 22 November 2014. From the velocity changes and recoveries observed at different depths, and susceptibility values previously estimated in rock experiments, we discuss the contributions of dynamic and static strain changes to the damage at the subsurface.

Methods/Experimental

We use data from Hi-net station N.MKGH and collocated KiK-net station NIGH17, 26 km from the epicenter of the N. Nagano earthquake (Fig. 1a). The Hi-net and KiK-net borehole sensors are installed at 150 m depth, while another KiK-net sensor is installed at the ground surface (Fig. 1b). A continuous record is available for Hi-net, while only event-triggered records are available for KiK-net. Both Hi-net and KiK-net systems sample ground oscillations at a frequency of 100 Hz. The frequency response of the Hi-net seismometer is flat from 1 to 30 Hz, while that of the KiK-net seismometer is flat from DC to about 20 Hz. Details of the Hi-net and KiK-net recording systems are summarized by Okada et al. (2004).

There are several Hi-net (KiK-net) stations around the source region of the N. Nagano earthquake. However, only E–W component data from stations N.MKGH and NIGH17 are available for combined analysis of KiK-net and Hi-net records, for reasons explained in the next section.

Processing of KiK-net records

We collect KiK-net seismograms for earthquakes that occurred between January 2009 and March 2015 (red circles in Fig. 1). We separate this time span into three periods: 25 January 2009 to 15 July 2014 (the reference period, before the N. Nagano earthquake), 23 November 2014 to 29 November 2014 (period 1, within 1 week of the N. Nagano earthquake), and 1 December 2014 to 24 March 2015 (period 2, 1 week to 4 months after the N.

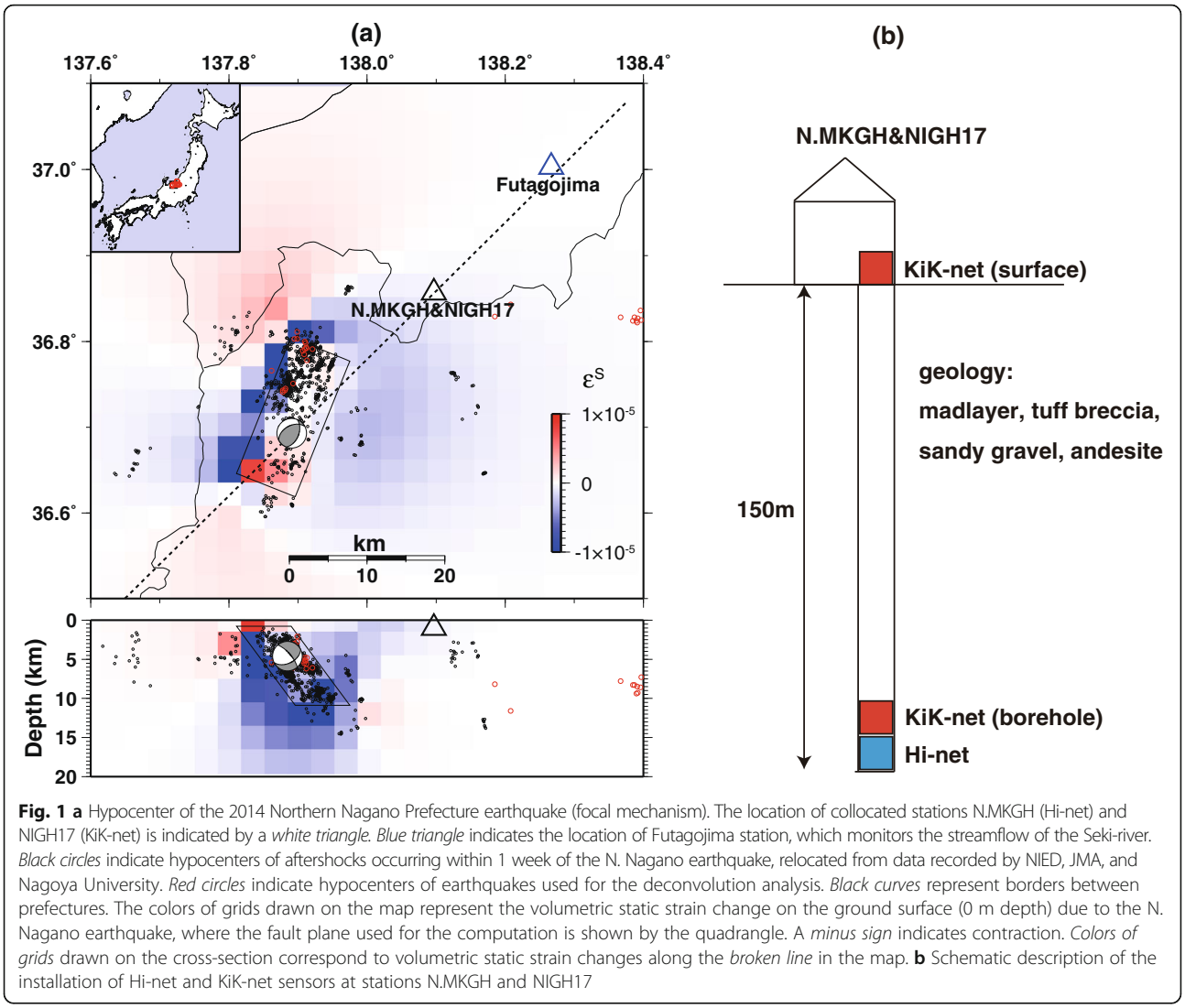

Fig. 1 a Hypocenter of the 2014 Northern Nagano Prefecture earthquake (focal mechanism). The location of collocated stations N.MKGH (Hi-net) and NIGH17 (KiK-net) is indicated by a *white triangle*. *Blue triangle* indicates the location of Futagojima station, which monitors the streamflow of the Seki-river. *Black circles* indicate hypocenters of aftershocks occurring within 1 week of the N. Nagano earthquake, relocated from data recorded by NIED, JMA, and Nagoya University. *Red circles* indicate hypocenters of earthquakes used for the deconvolution analysis. *Black curves* represent borders between prefectures. The colors of grids drawn on the map represent the volumetric static strain change on the ground surface (0 m depth) due to the N. Nagano earthquake, where the fault plane used for the computation is shown by the quadrangle. A *minus sign* indicates contraction. *Colors of grids* drawn on the cross-section correspond to volumetric static strain changes along the *broken line* in the map. **b** Schematic description of the installation of Hi-net and KiK-net sensors at stations N.MKGH and NIGH17

Nagano earthquake). To avoid apparent velocity changes due to variations in incidence angle, we select earthquake records that satisfy the condition that the S-wave incidence angle to the borehole bottom sensor is <22°. From each seismogram in each period, we extract a sequence of 10.24 s non-overlapping time windows that begins at the S-wave onset time and ends in the S-wave coda. We limit the value of the maximum dynamic strain (MDS) measured for each time window to smaller than 5×10^{-6} and larger than 5×10^{-9} for both the borehole bottom and the surface KiK-net sensors. Here, the maximum limit corresponds to the threshold of emergence of nonlinear site response effects (e.g., Beresnev and Wen 1996), and the minimum limit corresponds to about 10× the average amplitude of the ambient background noise. The MDS is computed by dividing the peak ground velocity (PGV) by the S-wave velocity in the medium, where V_{S30} and V_S at 150 m depth denote the S-wave velocities at the surface and the borehole bottom, respectively. For each windowed trace, we apply a 1–10 Hz 4-pole Butterworth bandpass filter to the surface/borehole deconvolution waveform (DCW). Then, we average all DCWs obtained in each period. The numbers of DCWs used for averaging in each period are 117, 55, and 30, for the reference period, period 1, and period 2, respectively.

Figure 2 shows the averaged DCWs for the E–W (Fig. 2a) and N–S (Fig. 2b) components of motion in each of the three time periods. The peaks of the DCWs, which appear around a lag time of 0.23 s, represent one-way S-wave travel times from the borehole bottom to the ground surface. The S-wave travel time computed from well logging data is 0.25 s. After the arrival of the peak, we see that reverberated waves, excited in the layers between the surface and the borehole bottom KiK-net sensor, appear in the DCWs.

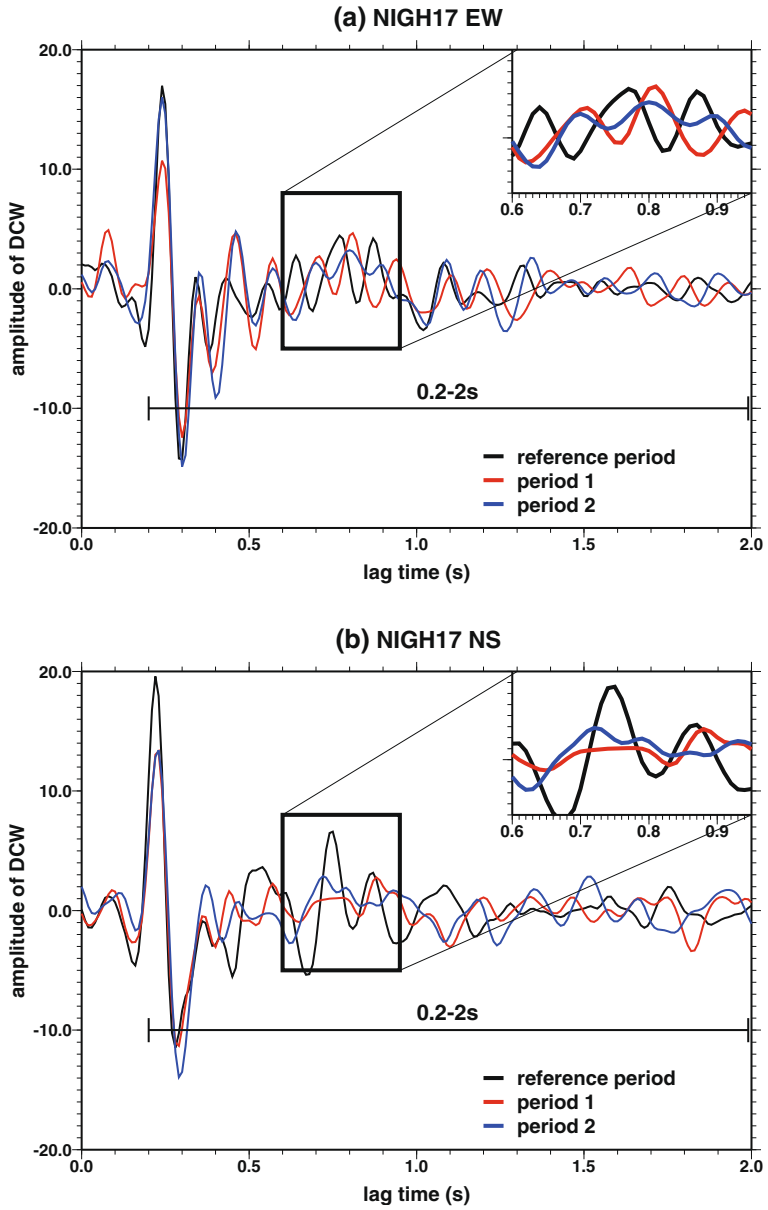

Fig. 2 Surface/borehole deconvolution waveforms (DCWs) for **a** E–W and **b** N–S components of motion obtained at KiK-net station NIGH17 in different periods (*black*: reference period, *red*: period 1, *blue*: period 2). Lag times of 0.2–2 s are used for the stretching technique

The waveforms of the E–W component are similar at different time periods; clear phase delays with respect to the reference period are recognized in periods 1 and 2. On the other hand, the waveforms of the N–S component are relatively dissimilar at different time periods. The shapes of the waveforms in periods 1 and 2 are considerably different from the shape of the reference period waveform. Because the recording system response and noise amplitude are almost the same for both components throughout the analyzed period, we consider that the N. Nagano earthquake excited anisotropic damage to the subsurface medium (e.g., Nakata and Snieder 2012), and consequently the DCW of the N–S component data changed more radically than that of the E–W component. Because the stretching technique (Wegler and Sens-Schönfelder 2007) is not applicable to a dissimilar waveform pair, we apply the stretching technique only to the E–W component to estimate the relative velocity change after the N. Nagano earthquake.

The lag time used for stretching begins at 0.2 s and ends at 2.0 s (see Fig. 2), within which the DCW is sensitive mostly to the medium between the two sensors

(<150 m depth). The error of the estimated relative velocity change is computed using the formula proposed by Weaver et al. (2011):

$$\mathrm{err} = \frac{\sqrt{1-C^2}}{2C}\sqrt{\frac{6\sqrt{\pi/2}T}{\omega_C^2(t_2^3-t_1^3)}}, \quad (1)$$

where C, T, ω_C, t_1, and t_2 are the maximum coherence value of the correlation coefficient, the inverse of the frequency bandwidth, the central angular frequency of the passband, and the start and end of the lag times used for the stretching technique, respectively.

Processing of Hi-net records

We first apply a 1–3 Hz 4-pole Butterworth bandpass filter to the E–W component of the Hi-net data, then apply one-bit normalization to suppress signals from earthquakes and other nonstationary phenomena. We then compute the autocorrelation function (ACF) using 1-hour time segments and average the ACFs obtained in each period. By applying the stretching technique to the ACFs obtained in the reference period to match the ACFs from periods 1 and 2, we compute the apparent relative velocity change after the N. Nagano earthquake. The lag time used for stretching begins at 4 s and ends at 12 s (see Fig. 3). Again, the error of the apparent relative velocity change is computed using Eq. (1).

Figure 3 shows the averaged ACFs obtained for each period. The inset figure shows a small phase delay in periods 1 and 2 with respect to the reference period, which can be attributed to a subsurface velocity reduction. Because the ACF can be regarded as the zero-offset Green's function (Claerbout 1968), the ACF at 4–12 s lag is sensitive to the medium change within about 20 km of the Hi-net sensor if we assume $V_S = 3.4$ km/s and single backscattering. Therefore, the velocity change near the fault zone (mostly >20 km from N.MKGH) is hardly sensed by the ACF for the range of lags considered. At this stage, we do not know how much of the change in the ACF can be attributed to the velocity changes below the installation depth (150 m) of the Hi-net sensor. It is necessary to evaluate the sensitivity of the ACF to estimate the velocity change below the installation depth; the procedure for this will be described later.

Correcting for seasonal velocity variations

Seismic velocity may exhibit seasonal variations (e.g., Meier et al. 2010) that are not caused by nonstationary phenomena like earthquakes. Figure 4a shows the variations in apparent relative velocity change from November 2009 to July 2015, where each point is a 1-week average of ACFs at station N.MKGH. In addition to the apparent velocity reductions after the Tohoku earthquake (M_W 9.0) on 11 March 2011, and the N. Nagano earthquake on 22 November 2014 (red arrows), the relative velocity changes show clear seasonal variations. Note that the RMS noise amplitude recorded at station N.MKGH (gray dots in Fig. 4) also shows a seasonal change, where the period of large RMS noise amplitude (April to May) corresponds to that of rapid velocity reduction and a low correlation coefficient. Because N.MKGH is located in a heavy snowfall zone, meltwater in spring induces strong streamflow and consequently may increase the amplitude of the ambient noise (e.g.,

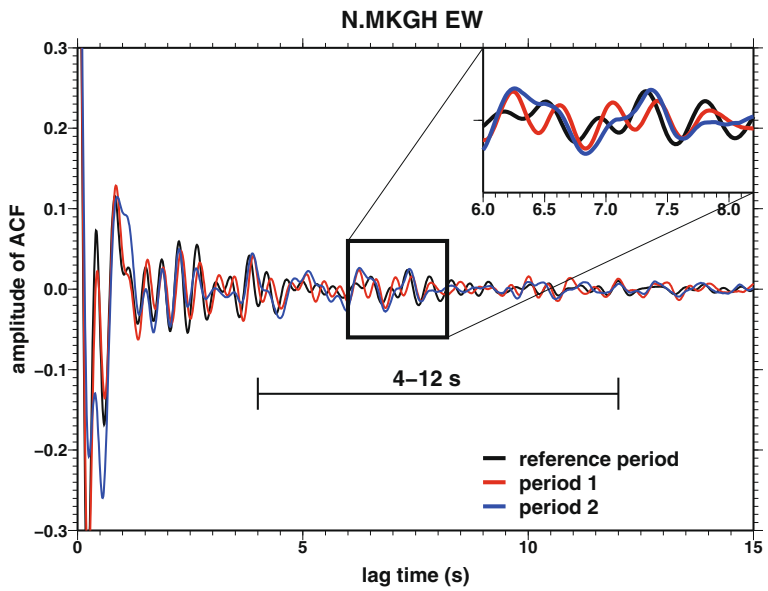

Fig. 3 Autocorrelation functions (ACFs) for E–W component data from Hi-net station N.MKGH in different periods (*black*: reference period, *red*: period 1, *blue*: period 2). Lag times of 4–12 s are used for the stretching technique

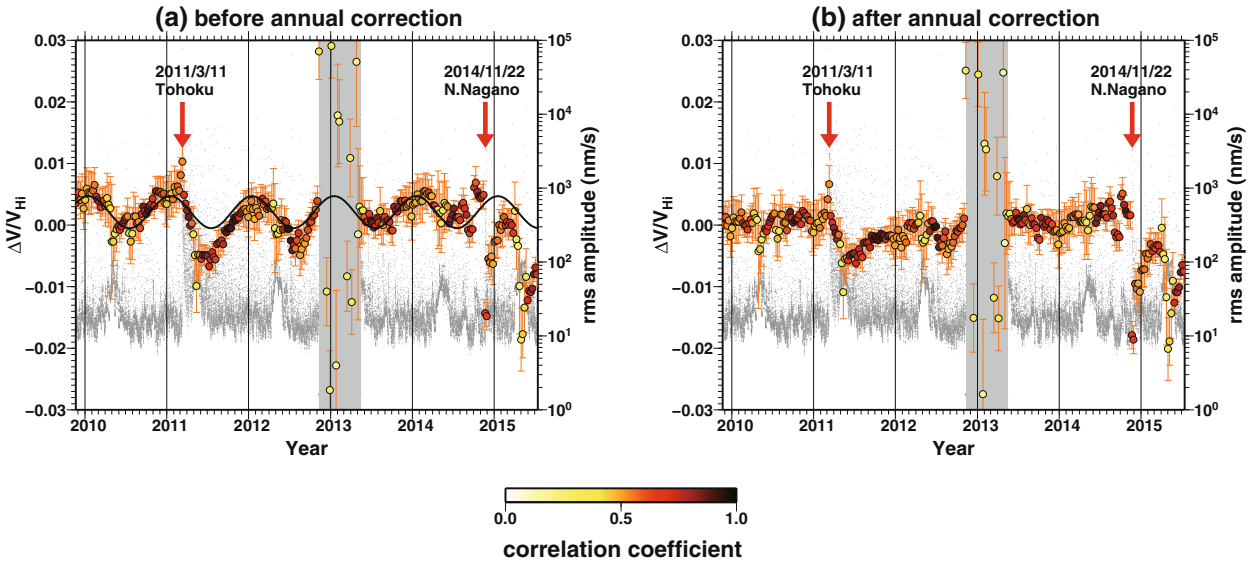

Fig. 4 Apparent relative velocity change **a** before and **b** after applying the seasonal corrections obtained from the ACFs recorded at Hi-net station N.MKGH. The *colors of the circles* indicate the correlation coefficients measured by the stretching technique. The *black sine curve* in Fig. 4a is fitted to seasonal variations. *Red arrows* indicate the origin times of the 2011 Tohoku and 2014 N. Nagano earthquakes. *Gray dots* represent one-hour averages of the RMS velocity amplitude in the 1–3 Hz passband of the E–W component of motion at station N.MKGH, where the measurement scale is given by the right ordinate. The area with a *gray background* indicates a period of recording system errors

Burtin et al. 2008). As shown in Fig. 5, a clear correlation is observed between the RMS noise amplitude (gray) and the streamflow of the Seki River at Futagojima monitoring station (blue, operated by the Ministry of Land, Infrastructure, Transport and Tourism, Japan; see Fig. 1), especially during the season of heavy streamflow (Fig. 5b). Therefore, the primary cause of the seasonal velocity variations is the change of the noise source distribution due to increased streamflow, and following changes in the groundwater system.

To separate earthquake-origin velocity changes from observed seasonal velocity changes, we fit a sine curve to the estimated seasonal velocity variations (e.g., Hobiger et al. 2012), excluding three time periods: within a year of the Tohoku earthquake (11 March 2011 to 11 March 2012), a period of recording system errors (10 November 2012 to 16 May 2013), and the post-N. Nagano earthquake period (22 November 2014 onward). We then subtract the sine curve from the raw data and use the subtracted data as the apparent relative velocity change (Fig. 4b). In addition to the velocity reductions due to the two large earthquakes, the corrected apparent relative velocity change also shows a large velocity reduction in April to May 2015. Although similar velocity reductions appear in this season every year, the 2015 case is much more significant than in other years and cannot be removed completely by subtraction of the fitted sine curve. One reason for this velocity reduction could be that the strong ground shaking and generation of cracks by the 2014 N. Nagano earthquake made the subsurface structure more susceptible to external changes, though this hypothesis is not supported by other observations. On the other hand, we do not correct the seasonal variations in velocity change obtained from the KiK-net DCWs because the data from KiK-net records are so sparse that seasonal variations cannot be confirmed.

Sensitivity of ACF to partial velocity changes

The relative velocity changes detected by the KiK-net DCWs and Hi-net ACFs ($\Delta V/V_{\mathrm{KiK}}$ and $\Delta V/V_{\mathrm{Hi}}$, respectively) are sensitive to velocity changes in different zones. The former is sensitive only to the medium at <150 m depth (the "shallow zone"), while the latter is sensitive to the medium both above and below 150 m depth (the latter is herein called the "deep zone"). To extract the velocity change in the deep zone from the values of $\Delta V/V_{\mathrm{KiK}}$ and $\Delta V/V_{\mathrm{Hi}}$, we evaluate the sensitivity of the ACF to partial velocity changes in the deep zone through a two-dimensional wave propagation simulation using the finite difference method (FDM). We do not perform a three-dimensional simulation because of the limitations of computation time. The most significant difference between 2D and 3D simulations that affects the sensitivity should be the S/P energy partition, which has values of 3.0 and 10.4 in an equilibrium state for the 2D and 3D cases, respectively (e.g., Sánchez-Sesma and Campillo 2006). Therefore, we apply

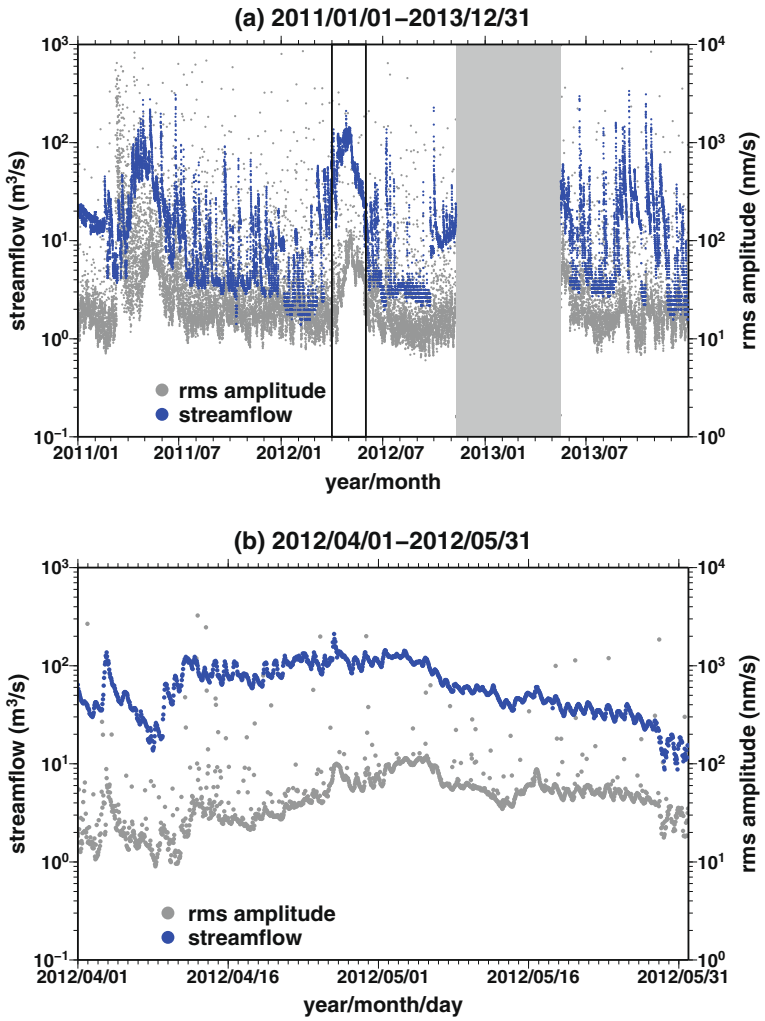

Fig. 5 a Comparison between RMS noise amplitude at station N.MKGH (*gray*) and streamflow of the Seki River at Futagojima monitoring station (*blue*) in the period from 1 January 2011 to 31 December 2013. The measurement scales of the RMS noise amplitude and the streamflow are given by the right and left ordinates, respectively. The area with a *gray background* indicates a period of recording system errors. **b** As for Fig. 5a, but for 1 April 2012 to 31 May 2012, indicated by a *black rectangle* in Fig. 5a

the same velocity perturbations for both V_P and V_S when evaluating the sensitivity, in order not to distinguish changes of V_P and V_S. The geometrical spreading factor is also different for the 2D and 3D cases; however, because we do not use waveform amplitude to evaluate sensitivity, these differences will not affect our outcome significantly.

We assume that the ACF of the Hi-net ambient noise records approximately represents the Green's function (Claerbout 1968), where both the source and the receiver are located at the position of the Hi-net sensor (150 m depth). We note that the passive image interferometry technique is available for time-lapse monitoring if the noise source distribution is temporally stable, even though the spatial distribution of the noise source may not be uniform and the Green's function may not be correctly retrieved (Hadziioannou et al. 2009). Since possible bias due to seasonal variations in the noise source distribution would be corrected by the procedure explained in the previous section, using the numerical Green's function to approximate the observed ACF is appropriate for our purposes. Therefore, we set a horizontal single point force at 150 m depth and reproduce the horizontal waveform at the same location (Fig. 6a), which is regarded as the corresponding ACF. We use a Küpper wavelet with a central frequency of 2 Hz as the source-time function considering the 1 to 3 Hz bandpass filter applied to the observed Hi-net record.

For the medium below 2.5 km, the background 1D velocity structure is estimated from the results of

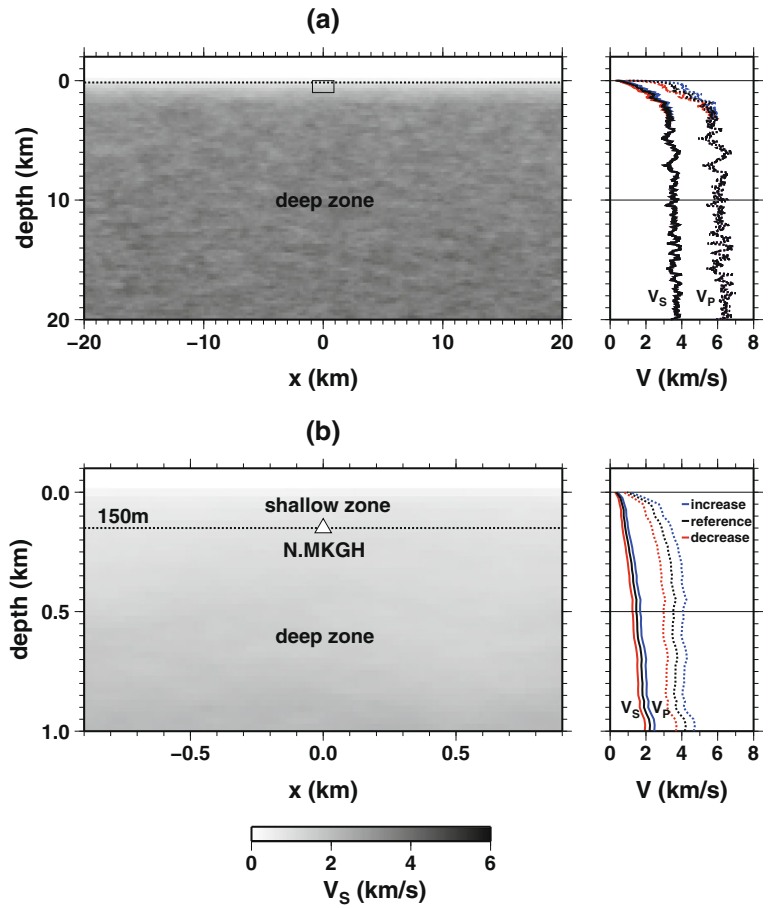

Fig. 6 Example of **a** a cross-section and 1D profile of the reference velocity structure used in the FDM wave propagation simulation, and **b** a magnified image of the area *surrounded by the rectangle* in Fig. 6a. The source and receiver are set at 150 m depth, as shown by the *triangle*. Colored 1D velocity profiles represent increased (*blue*) and decreased (*red*) reference velocity structures, which are used to constrain the range of sensitivities *a* due to uncertainty in the background velocity model

velocity tomography by Matsubara and Obara (2011). For the shallower medium, we use well log data from station NIGH17 with a deep subsurface structure model provided by J-SHIS (Fujiwara et al. 2009). We then generate five 2D velocity structures by superimposing five seeds of exponential-type random velocity fluctuations (e.g., Sato et al. 2012) on the 1D velocity structure. For random fluctuation parameters, we set $\varepsilon = 0.06$ (fractional velocity fluctuation), $a_x = 600$ m (horizontal correlation length), and $a_z = 200$ m (vertical correlation length), based on field measurements by Holliger and Levander (1992). The quality factor Q is adopted from the 1D reference model provided by J-SHIS. The mass density of the medium is $\rho = 310\ V_P^{0.25}$ following the empirical formula of Gardner et al. (1974), where the measurement units of ρ and V_P are kg/m^3 and m/s, respectively. Figure 6 shows an example of the velocity profile used in the numerical simulations. The model covers a horizontal region of 100 km to a depth of 50 km (not shown fully in Fig. 6) and is discretized in grid intervals of 25 m. Free surface and absorbing boundary conditions are employed for the top surface ($z = 0$ km) and the other three boundaries of the computation area, respectively; these conditions avoid numerical divergence and numerical dispersion. The temporal sampling interval is 0.0015 s.

To evaluate the sensitivity of the ACF to partial velocity changes, the numerical waveforms are computed for the reference and perturbed velocity structures. The perturbed structures are reconstructed by applying a 3% velocity reduction to the reference medium at depths of 0–150 m (above the location of the sensor) and 150 m to 50 km (below the location of the sensor) individually. We call these zones the "shallow" and "deep" zones, respectively, as shown in Fig. 6b. Applying the stretching technique to the reference and perturbed waveforms using lag times of 4–12 s, we compute the travel time shifts τ_{shallow} and τ_{deep} due to the 3% velocity reductions in the shallow and

deep zones, respectively. The sensitivity to the deep zone α is given by

$$\alpha = \frac{\tau_{\mathrm{deep}}}{\tau_{\mathrm{shallow}} + \tau_{\mathrm{deep}}}. \quad (2)$$

We consider that the observed relative velocity change $\Delta V/V_{\mathrm{Hi}}$ is approximately given by the weighted sum of the partial relative velocity changes,

$$\frac{\Delta V}{V}_{\mathrm{Hi}} \approx (1-\alpha)\frac{\Delta V}{V}_{\mathrm{shallow}} + \alpha\frac{\Delta V}{V}_{\mathrm{deep}}, \quad (3)$$

where $\Delta V/V_{\mathrm{deep}}$ and $\Delta V/V_{\mathrm{shallow}}$ represent the true relative velocity changes in the deep and shallow zones, respectively. Equation (3) is a good approximation when the relative velocity change is much smaller than unity (e.g., Snieder 2006; see also Appendix A). Because $\Delta V/V_{\mathrm{Hi}}$ and $\Delta V/V_{\mathrm{shallow}}(=\Delta V/V_{\mathrm{KiK}})$ are obtained directly from the observations, we can estimate the value of $\Delta V/V_{\mathrm{deep}}$ once we obtain the sensitivity α.

Results and Discussion

The evaluated sensitivity α is 0.78 under the reference velocity structure. This value indicates that almost 80% of the ACF energy senses changes in the medium below the Hi-net sensor installation depth of 150 m. Using this α value and Eq. (3), we plot $\Delta V/V_{\mathrm{deep}}$ in Fig. 7 (blue circles), as well as the relative velocity change detected from the DCW of the KiK-net records ($\Delta V/V_{\mathrm{shallow}}$, red circles) and from the ACF of the Hi-net records ($\Delta V/V_{\mathrm{Hi}}$, black circles). In period 1, the estimated relative velocity changes are −3.1 and −1.4% in the shallow and deep zones, respectively. In period 2, the relative velocity changes recover to −1.9 and −1.1% in the shallow and deep zones, respectively.

The value of $\alpha = 0.78$ is evaluated using the reference velocity structure, which may include biases from the true velocity structure. Therefore, it is important to evaluate how much the α value could be perturbed due to uncertainty in the reference velocity structure. We verify the range of sensitivities α using different reference velocity structures reproduced by decreasing and increasing the reference velocities above 2.5 km depth by up to 20%, as shown by the red and blue 1D velocity profiles in Fig. 6, respectively. The evaluated α values are 0.75 and 0.82 for decreased and increased velocities, respectively. As the velocity of the shallow zone decreases, more of the energy of the ACF is trapped by the shallow layers; consequently, the ACF becomes more sensitive to the velocity change in the shallow zone and the α value decreases.

Using Eq. (3), we draw the α dependence of $\Delta V/V_{\mathrm{deep}}$ in Fig. 8, where $\Delta V/V_{\mathrm{shallow}}$ and $\Delta V/V_{\mathrm{Hi}}$ are fixed at the observed values. As derived from Eq. (3), the value of

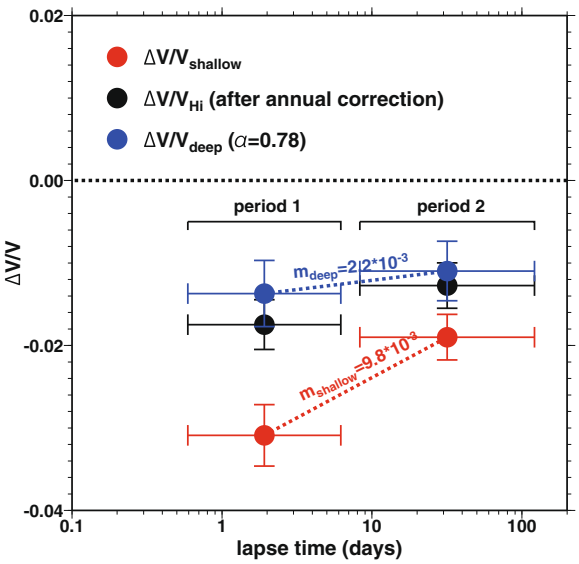

Fig. 7 Relative velocity changes estimated for the shallow (*red circles*) and deep (*blue circles*) zones, where $a = 0.78$ is used for the latter. Relative velocity changes detected from the Hi-net ACF are shown by *black circles*. The *abscissa* indicates the lapse time after the N. Nagano earthquake, plotted with a logarithmic scale. The *m* values in the figure represent log(*t*)-recovery speeds, calculated using Eq. (5)

$\Delta V/V_{\mathrm{deep}}$ is equal to $\Delta V/V_{\mathrm{Hi}}$ when $\alpha = 1$. In this case, the ACF is sensitive only to the velocity change in the deep zone. As α becomes smaller, $\Delta V/V_{\mathrm{deep}}$ and its standard deviation increase, and both diverge to infinity when $\alpha = 0$. In this case, the ACF has no sensitivity to change in the deep zone, which means we cannot obtain any information about the velocity change below 150 m. From Fig. 8, we confirm that the value of $\Delta V/V_{\mathrm{deep}}$ does not change drastically within the evaluated range of α (from 0.75 to 0.82, as indicated by the white background).

Contribution of dynamic and static strain changes to velocity change

To investigate the cause of the velocity changes observed at different depths, we now examine the contributions of dynamic and static strain changes due to the N. Nagano earthquake as the candidate of the cause.

For the N. Nagano earthquake, the maximum dynamic strains (MDS) recorded at station NIGH17 are $\varepsilon^{D}_{\mathrm{surface}} = 5.3 \times 10^{-4}$ and $\varepsilon^{D}_{\mathrm{borehole}} = 1.4 \times 10^{-4}$ at the surface and the borehole bottom, respectively. These values can constrain the range of the MDS in the shallow zone. In the deep zone, on the other hand, we indirectly evaluate the MDS through the results of the numerical wave propagation simulation. Using the reference velocity structure shown in Fig. 6 and setting a 0.5 Hz Küpper wavelet as a source waveform (since 0.5 Hz is the

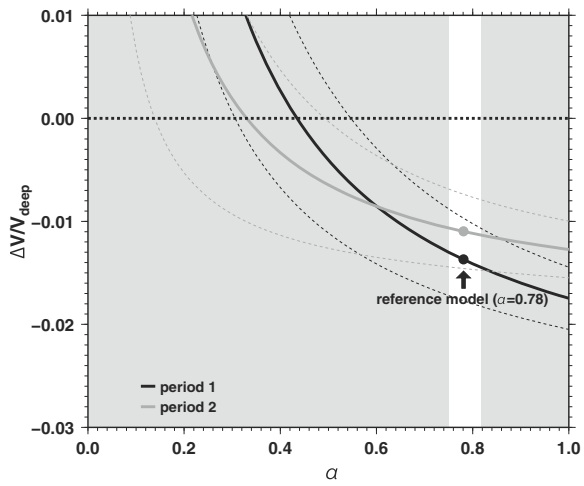

Fig. 8 α value-dependence of the relative velocity change in the deep zone. The *black and gray curves* represent values evaluated in periods 1 and 2, respectively. *Broken curves* represent the ranges of the corresponding error bars. The area with a *white background* represents a range of α values evaluated using the decreased ($\alpha = 0.75$) and increased ($\alpha = 0.82$) reference velocity structures

dominant frequency of the observed velocity seismogram) to the position that corresponds to the hypocenter of the N. Nagano earthquake ($x = -25.9$ km, $z = 4.6$ km), we synthesize the numerical waveforms of the horizontal component at positions $x = 0$ km, $z = 150$ m and $x = 0$ km, $z = 5$ km. The 5 km depth is considered because below which the ACF has almost no sensitivity, according to our numerical tests. We obtain a ratio of computed MDS values at 5 km depth/MDS at 150 m depth of $\varepsilon^D_{5\mathrm{km}}/\varepsilon^D_{150\mathrm{m}} = 0.091$. We then calculate an MDS value at 5 km depth of $\varepsilon^D_{5\mathrm{km}} = 0.091 \times \varepsilon^D_{\mathrm{borehole}} = 1.3 \times 10^{-5}$ for the N. Nagano earthquake. We note that this evaluation may include a large bias due to the difference between geometrical spreading factors for the 2D (numerically simulated) and 3D (observed) media. Using these values, we evaluate the possible ranges of MDS values in the shallow and deep zones as $1.4 \times 10^{-4} \le \varepsilon^D_{\mathrm{shallow}} \le 5.3 \times 10^{-4}$ and $1.3 \times 10^{-5} \le \varepsilon^D_{\mathrm{deep}} \le 1.4 \times 10^{-4}$, respectively.

Next, we compute the coseismic static strain change beneath station N.MKGH using the code of Okada (1992) and a rectangular plane fault model (20 km long and 14 km width) for the N. Nagano earthquake (quadrangle in Fig. 1). Here, the focal mechanism is adopted from the CMT solution (strike = 22°, dip = 51°, rake = 62°) of F-net (the Full Range Seismograph Network of Japan, operated by NIED). A slip of 0.4 m is uniformly distributed on the rectangular fault. The corresponding seismic moment is 3.4×10^{18} (Nm) = M_W 6.3, which is close to the reported value. Our computed ranges of the static volumetric strain change (SVSC) are $-3.73 \times 10^{-7} \le \varepsilon^S_{\mathrm{shallow}} \le -3.68 \times 10^{-7}$ and $-3.7 \times 10^{-7} \le \varepsilon^S_{\mathrm{deep}} \le -1.5 \times 10^{-7}$ in the shallow (0–150 m depth) and deep (150 m–5 km) zones, respectively, where the minus sign indicates contraction. The distributions of SVSC are mapped in Fig. 1a by colored grids.

Figure 9 compares the observed relative velocity change in period 1 and the evaluated ranges of MDS (solid circles) and SVSC (open symbols) in the shallow and deep zones. Although the evaluated SVSC has negative values, we show their absolute values in Fig. 9 for the sake of discussion. The values of MDS are larger than SVSC in both the shallow and deep zones by ~10^2–10^3. In the same figure, we also show the values of susceptibility (relative velocity change with respect to the applied strain change, given by $\Delta V/V/\varepsilon$) with gray curves. If the observed velocity reduction is caused mainly by the dynamic strain change, then the value of susceptibility should be approximately −1000 to −100 for both zones. On the other hand, if the observed velocity reduction is caused mostly by the static strain change, then the susceptibility should be around -10^5.

We now compare these calculated values with susceptibilities measured in rock experiments. According to Prioul et al. (2004), the values of the third-order elastic constants (TOE), which give the variability of material with respect to the applied static stress change (e.g.,

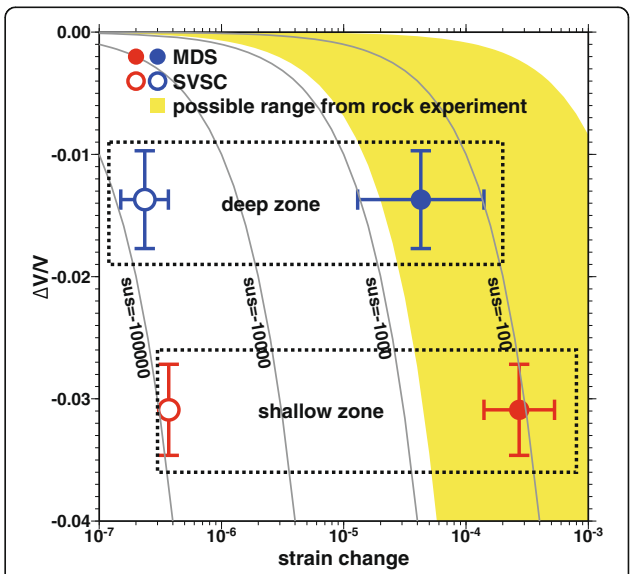

Fig. 9 Relationship between the observed relative velocity change $\Delta V/V$ in period 1, and dynamic (*solid circles*) and static (*open symbols*) strain changes in the shallow and deep zones at station N.MKGH. *Gray curves* represent susceptibility contours defined by $\Delta V/V/\varepsilon$. The area covered by the *yellow background* represents the possible range of susceptibilities, $-688 < \Delta V/V/\varepsilon < -8$, within a depth range of 200 to 4000 m, as indicated by the rock experiments of Prioul et al. (2004)

Murnaghan 1967), are $c_{111} = -11300$, $c_{123} = 5800$, and $c_{111} = -3100$ GPa, $c_{123} = 40$ GPa under hydrostatic stresses of 5–30 and 30–100 MPa, respectively, for a rock sample of North Sea Shale (Table 2 of Prioul et al. 2004). Because hydrostatic stresses of 5–100 MPa correspond to depths of ~200–4000 m, these values are applicable to the medium in the deep zone. Using these TOE values, the susceptibility is given by

$$\frac{\Delta V/V^S}{\varepsilon} = \frac{1}{12c_{44}}(c_{111}-c_{123}) + \frac{1}{2}, \tag{4}$$

where c_{44} is the shear modulus. Equation (4) is derived by modifying the second formula of Eq. (13) of Sawazaki et al. (2015), where we took the average of the relative S-wave velocity change for all three propagation directions; i.e., $\Delta V/V^S = (\Delta V_{S12}/V + \Delta V_{S23}/V + \Delta V_{S31}/V)/3$. Using Eq. (4), the TOE constants from Prioul et al. (2004) and the c_{44} (shear modulus) value at depths of 200 to 4000 m, we calculate a possible range of susceptibilities of −688 to −8 in the deep zone. This range is drawn in yellow in Fig. 9; it mostly covers the estimations from the MDS, but does not cover the estimates from the SVSC. Because the TOE constants measured by Prioul et al. (2004) are obtained for loading of the static strain change, we admit that these values are not necessarily applicable to loading of the dynamic strain change. Also, we note that the well log core sample at station NIGH17 is composed of a mixture of topsoil, tuff breccia, sandy gravel, and andesite (see Fig. 1b), which is not necessarily similar to the North Sea Shale used by Prioul et al. (2004). Nevertheless, we think that the dynamic strain change is more likely to be the primary cause of the velocity reduction than static strain change, because the susceptibilities evaluated from the static strain change are completely outside of the possible range of the rock experiments.

Cause of velocity recovery

The velocity recovery also appears differently in the shallow and deep zones, as the shallow zone recovers more quickly. We consider that "slow dynamics" (i.e., the behavior of material that slowly approaches its equilibrium state; originally presented in the rock experiments such as TenCate et al. 2000) is a convincing mechanism that can explain the observed velocity recovery.

Firstly, we note that the horizontal static displacement due to 3 months of postseismic deformation is less than 4% of the estimated coseismic deformation (Yarai et al. 2015). Because the estimated coseismic static strain change is on the order of 10^{-7}–10^{-6}, the static strain change due to postseismic deformation is on the order of 10^{-8}. Such a small strain change alone cannot explain an observed velocity recovery of up to 30% in the shallow zone. Therefore, we exclude postseismic deformation as the primary cause of the observed velocity recovery.

According to the rock experiments of TenCate et al. (2000), the relative resonance frequency shift of a rock sample, $\Delta f/f$, recovers in proportion to the logarithm of the lapse time t after unloading a dynamic strain, as follows:

$$\frac{\Delta f(t) - \Delta f(t_0)}{f} = m \log_{10}\left(\frac{t}{t_0}\right), \tag{5}$$

where t_0 and m are the reference time and the parameter that controls the speed of the recovery, respectively. This log(t)-type recovery has been widely confirmed by field data (e.g., Sawazaki et al. 2009; Gassenmeier et al. 2016). Applying Eq. (5) to the observed relative velocity changes shown in Fig. 7, where the relative velocity change is used instead of the relative resonance frequency shift because they are equivalent, we obtain m values of $(9.8 \pm 3.8) \times 10^{-3}$ and $(2.2 \pm 4.4) \times 10^{-3}$ in the shallow and deep zones, respectively. These values are plotted in Fig. 10 along with the m–ε^D relationship $m \cong 11.1 \times (|\varepsilon^D| - 4.7 \times 10^{-7})$ obtained by TenCate et al. (2000). We note that their experiment was carried out for dynamic strains ranging from 4.0×10^{-7} to 2.64×10^{-6} (gray solid curve in Fig. 10), which are much smaller than the estimated MDS values in our study. Although the error range is large, especially for the deep zone, the m values obtained in our study seem to lie along the extrapolation curve of TenCate et al.'s (2000) empirical relationship (gray broken curve in Fig. 10). This result indicates that a similar recovery mechanism underlies both the laboratory scale (centimeters) and field scale (hundreds of meters), and the recovery rate is controlled primarily by the strength of the applied MDS.

The MDS dependence of the recovery rate can be explained as follows. After unloading the dynamic strain, the actual contact area on the surface of microcracks begins to increase through a creep-like deformation process. As the actual contact area becomes larger, the normal stress applied to the contact area becomes smaller and the rate of the deformation decreases. This decelerates the expansion of the actual contact area. As a consequence of this feedback process, the initial contact area controls the average deformation speed: if the initial contact area is smaller, then the deformation speed is faster (e.g., Brechet and Estrin 1994). Because the initial contact area is related to damage in the medium, which would be excited more by stronger dynamic strains, the recovery speed will be faster for the material affected by a larger MDS.

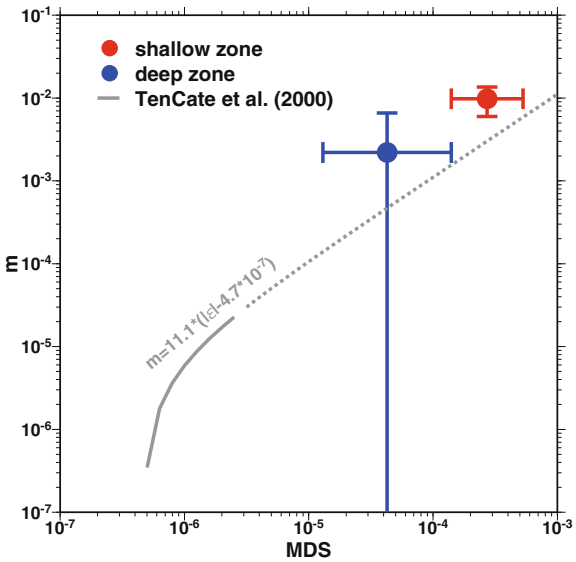

Fig. 10 Relationship between the observed velocity recovery rate *m* and the MDS in the shallow and deep zones at station N.MKGH. *Gray curve* represents the empirical relationship proposed by TenCate et al. (2000), where the *solid and broken curves* are the corresponding ranges examined in the rock experiment and their extrapolations, respectively

Other factors that control velocity change and recovery

As stated above, we consider that the observed velocity reduction is controlled mainly by damage due to the dynamic strain change, and recovery is controlled by healing of microcracks, analogous to slow dynamics. However, we note that this explanation is only applicable to areas distant from the faulting zone (>20 km). Because dynamic and static strains attenuate geometrically following r^{-2} and r^{-3}, respectively, where r is the distance from the hypocenter (Aki and Richards 2002), the contribution of the static strain change due to coseismic deformation would be non-negligible near the fault zone. For the same reason, the static strain change due to postseismic deformation may also contribute to velocity recovery near the fault zone (e.g., Brenguier et al. 2008). Another important factor in the recovery process is aftershocks. Because the magnitude of the largest aftershock during period 2 was only 4.4 for the N. Nagano case, we do not consider additional damage from aftershocks. However, if aftershocks are large and active, secondary damage from large aftershocks could cause additional velocity reduction (Rubinstein and Beroza 2004) and recovery speed could be slowed. Thus, the contributions of dynamic and static strain changes may depend on both distance from the fault zone and aftershock activity. If these factors are contaminated, the features of the velocity change and the recovery processes will become more complex.

We also need to consider that if the damage in the medium is severe and the shapes of the DCWs and ACFs before and after the mainshock become dissimilar, a stretching technique might be inapplicable. For such cases, an irreversible medium change would be excited and the recovery process would be different from the case of weaker damage. In fact, in this study, the peak amplitude of the DCW mostly recovers to pre-mainshock level in period 2 for the E–W component (Fig. 2a), but not for the N–S component (Fig. 2b). This indicates that the N–S component was more severely damaged by the N. Nagano earthquake than the E–W component.

Because we examined only one station for one earthquake, it is important to collect case studies of velocity changes at different depths for different situations. In particular, a comparison between the case of significant strong motion with small crustal deformation (e.g., a large, deep earthquake) and that of large crustal deformation without seismic motion (e.g., a slow earthquake) is interesting. Because the susceptibility of the subsurface medium and recovery speed may each differ due to conditions in the medium, such as temperature, confined stress, saturation ratio, and permeability (e.g., Brenguier et al. 2014), it is also important to perform time-lapse velocity monitoring at a variety of sites.

Conclusions

We computed seismic velocity changes associated with the 2014 Northern Nagano Prefecture earthquake (M_W 6.2) at different depths by applying passive image interferometry to co-located seismograms from Hi-net and KiK-net stations. Using numerical wave propagation simulations, we evaluated the sensitivity of the Hi-net ambient noise ACF to velocity changes in the medium below 150 m depth. The detected relative velocity changes are −3.1% above 150 m depth and −1.4% below 150 m depth within 1 week of the N. Nagano earthquake. The relative velocity changes recover to −1.9 and −1.1% in the period from 1 week to 4 months after the N. Nagano earthquake. Examining the dynamic and static strain changes estimated for the N. Nagano earthquake, and the susceptibilities measured in rock experiments, we conclude that the primary cause of the velocity change is dynamic strain change due to the mainshock, rather than static strain change, at a location farther than 20 km from the mainshock fault. The recovery speed is faster in the shallow zone than in the deep zone, probably because the healing speed of microcracks is controlled by the initial damage in the medium. This behavior is analogous to slow dynamics observed in rock experiments.

Data

Hi-net and KiK-net records are available through the NIED web portal (http://www.hinet.bosai.go.jp/?LANG=en and

http://www.kyoshin.bosai.go.jp/, respectively). CMT solutions for F-net data are available from the NIED website (http://www.fnet.bosai.go.jp/event/search.php?LANG=en). Streamflow records are available from the webpage of the Water Information System of the Ministry of Land, Infrastructure, Transport and Tourism, Japan (http://www1.river.go.jp/; in Japanese).

Appendix

Here, we derive Eqs. (2) and (3) from the main text. The derivation is adapted in part from Snieder (2006).

The travel time t_P of a seismic wave that propagates along a path P is given by

$$t_P = \int_P \frac{1}{v(\mathbf{r})} ds, \tag{A1}$$

where $v(\mathbf{r})$ is the reference velocity at position $\mathbf{r}$. We consider that the whole space is divided into regions A and B, as shown in Figure 11 of Appendix. Although the whole space is separated vertically in Figure 11 of Appendix for convenience, the following derivation holds for arbitrary separations. Assuming that the velocity of the medium is perturbed by a constant ratio $\delta v_0/v$ ($|\delta v_0/v| < < 1$) in region A, we define a velocity perturbation function $\delta v_A(\mathbf{r})$ as

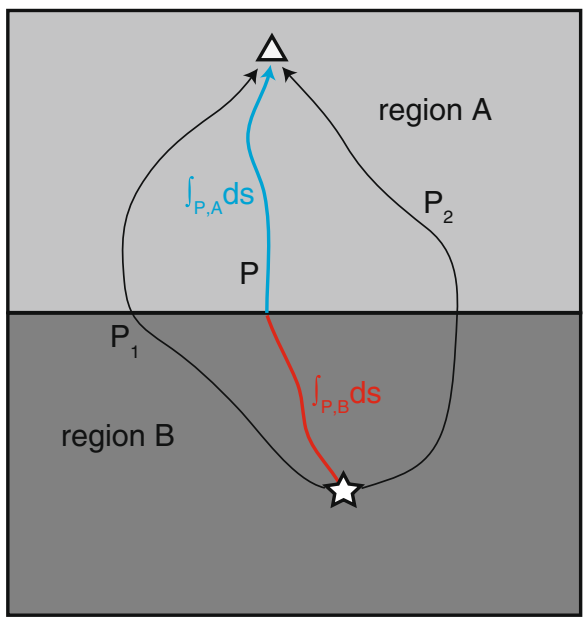

Fig. 11 Schematic illustration that describes the separation of the whole medium into regions A and B. The curves P_i represent paths along which seismic waves propagate, where i indicates the path number. $\int_{P,A} ds$ and $\int_{P,B} ds$ are integrals along path P that pass through regions A and B, respectively

$$\delta v_A(\mathbf{r}) = \begin{cases} \dfrac{\delta v_0}{v} v(\mathbf{r}) & \text{inside region } A \\ 0 & \text{inside region } B \end{cases}. \tag{A2}$$

The travel time shift $\tau_{P,A}$ due to this velocity perturbation is given by

$$t_P + \tau_{P,A} = \int_P \frac{1}{v(\mathbf{r}) + \delta v_A(\mathbf{r})} ds \approx \int_{P,A} \left(\frac{1}{v(\mathbf{r})} - \frac{1}{v(\mathbf{r})} \frac{\delta v_0}{v} \right) ds + \int_{P,B} \frac{1}{v(\mathbf{r})} ds \tau_{P,A} \approx - \frac{\delta v_0}{v} \int_{P,A} \frac{1}{v(\mathbf{r})} ds, \tag{A3}$$

where the path integrals in regions A and B satisfy

$$\int_{P,A} (\cdots) ds + \int_{P,B} (\cdots) ds = \int_P (\cdots) ds. \tag{A4}$$

The change in path P due to the velocity perturbation is negligible because the magnitude of the velocity perturbation is much smaller than the reference velocity. In the same way, the travel time shift $\tau_{P,B}$ due to the velocity perturbation function

$$\delta v_B(\mathbf{r}) = \begin{cases} 0 & \text{inside region } A \\ \dfrac{\delta v_0}{v} v(\mathbf{r}) & \text{inside region } B \end{cases} \tag{A5}$$

is given by

$$\tau_{P,B} \approx - \frac{\delta v_0}{v} \int_{P,B} \frac{1}{v(\mathbf{r})} ds. \tag{A6}$$

Using Eqs. (A1), (A3), and (A6), we obtain

$$\tau_{P,A} + \tau_{P,B} \approx - \frac{\delta v_0}{v} \int_P \frac{1}{v(\mathbf{r})} ds = - \frac{\delta v_0}{v} t_P. \tag{A7}$$

We now consider that the velocity of the medium is perturbed by constant ratios $c_A \delta v_0/v$ and $c_B \delta v_0/v$ in regions A and B, respectively, where c_A and c_B are arbitrary constants that satisfy $|c_A \delta v_0/v| < < 1$ and $|c_B \delta v_0/v| < < 1$, respectively. The travel time shift due to these velocity perturbations is given by

$$\tau_{P, c_A A + c_B B} \approx - c_A \frac{\delta v_0}{v} \int_{P,A} \frac{1}{v(\mathbf{r})} ds - c_B \frac{\delta v_0}{v} \int_{P,B} \frac{1}{v(\mathbf{r})} ds = c_A \tau_{P,A} + c_B \tau_{P,B}. \tag{A8}$$

Because the observed wavefield is represented as a superposition of the waves that propagate along all possible paths distributed in a space (P_i in Figure 11 of Appendix), the observed travel time shift $\overline{\tau}$ of the wavefield is given by the weighted average of the travel time shifts for all waves (Snieder 2006), as follows:

$$\overline{\tau} = \frac{\sum_P \tau_P I_P}{\sum_P I_P}, \tag{A9}$$

where I_P is the intensity of the wave that propagates along path P. Using Eqs. (A7), (A8), and (A9), we obtain

$$\begin{aligned}\overline{\tau}_A + \overline{\tau}_B &= \frac{\sum_P \left(\tau_{P,A} + \tau_{P,B}\right) I_P}{\sum_P I_P} \\ &= -\frac{\delta v_0}{v} \frac{\sum_P t_P I_P}{\sum_P I_P} = -\frac{\delta v_0}{v} \overline{t},\end{aligned} \tag{A10}$$

and

$$\overline{\tau}_{c_A A + c_B B} = \frac{\sum_P \tau_{P,c_A A + c_B B} I_P}{\frac{\sum_P I_{P \approx c_A} \sum_P \tau_{P,A} I_P}{\sum_P I_{P+c_B}} \sum_P \tau_{P,B} I_P}{\sum_P I_{P = c_A \overline{\tau}_A + c_B \overline{\tau}_B}}} \tag{A11}$$

Using Eqs. (A10) and (A11), we obtain

$$\begin{aligned}\overline{\tau}_{c_A A + c_B B} \overline{t} &= c_A \overline{\tau}_A + c_B \overline{\tau}_B \overline{t} \\ &= -(1-\alpha) \frac{c_A \delta v_0}{v} - \alpha \frac{c_B \delta v_0}{v},\end{aligned} \tag{A12}$$

where

$$\alpha = \frac{\overline{\tau}_B}{\overline{\tau}_A + \overline{\tau}_B}. \tag{A13}$$

In the main text, we regarded $\overline{\tau}_A$ and $\overline{\tau}_B$ as travel time shifts due to 3% partial velocity reductions in the shallow (region A) and deep (region B) zones, respectively, and regarded $c_A \delta v_0 / v$ and $c_B \delta v_0 / v$ as the true relative velocity changes in the shallow and deep zones, respectively. We also consider that the apparent relative velocity change obtained from the Hi-net ACF is measured using the stretching technique, which implicitly uses

$$\left(\frac{\Delta V}{V}\right)_{\mathrm{Hi}} = -\overline{\tau}_{c_A A + c_B B} \overline{t}. \tag{A14}$$

From Eqs. (A12), (A13), and (A14), we obtain Eqs. (2) and (3) in the main text.

Abbreviations

ACF: Autocorrelation function; DCW: Deconvolved waveform; FDM: Finite difference method; Hi-net: High-sensitivity seismograph network of Japan; KiK-net: Kiban Kyoshin strong-motion seismograph network of Japan; MDS: Maximum dynamic strain; NIED: National Research Institute for Earth Science and Disaster Resilience, Japan; PGV: Peak ground velocity; SVSC: Static volumetric strain change; TOE: Third-order elastic constants

Acknowledgements

We thank the Ministry of Land, Infrastructure, Transport and Tourism, Japan, for allowing us to use their streamflow data. Dr. T. Yano provided the relocated aftershock event catalog. We also thank Dr. T. Tanimoto, editor of *Progress in Earth and Planetary Science*, and Dr. C. Hadziioannou and one anonymous reviewer for their thoughtful comments that improved the manuscript. Seismic Analysis Code (SAC; Goldstein and Snoke 2005) and Generic Mapping Tools (GMT; Wessel et al. 2013) were used for signal processing and for constructing figures, respectively.

Funding

Not applicable.

Authors' contributions

KS analyzed the data and drafted the manuscript. TS, TU, and KS provided many comments and suggestions to improve the manuscript. All authors read and approved the final manuscript.

Competing interests

The authors declare that they have no competing interests.

Received: 21 April 2016 Accepted: 7 November 2016
Published online: 22 November 2016

References

Aki K, Richards PG (2002) Quantitative seismology. Univ. Sci. Books, Sausalito, p 700

Beresnev IA, Wen KL (1996) Nonlinear soil response—a reality? Bull Seismol Soc Am 86(6):1964–1978

Brechet Y, Estrin Y (1994) The effect of strain rate sensitivity on dynamic friction of metals. Scr Metall Mater 30(11):1449–1454

Brenguier F, Campillo M, Hadziioannou C, Shapiro NM, Nadeau RM, Larose E (2008) Postseismic relaxation along the San Andreas Fault at Parkfield from continuous seismological observations. Science 321:1478–1481. doi:10.1126/science.1160943

Brenguier F, Campillo M, Takeda T, Aoki Y, Shapiro NM, Briand X, Emoto K, Miyake H (2014) Mapping pressurized volcanic fluids from induced crustal seismic velocity drops. Science 345(6192):80–82

Burtin A, Bollinger L, Vergne J, Cattin R, Nábělek JL (2008) Spectral analysis of seismic noise induced by rivers: a new tool to monitor spatiotemporal changes in stream hydrodynamics. J Geophys Res 113:B05301. doi:10.1029/2007JB005034

Claerbout JF (1968) Synthesis of a layered medium from its acoustic transmission response. Geophysics 33(2):264–269

Fujiwara H, Kawai S, Aoi S, Morikawa N, Senna S, Kudo N, Ooi M, Hao KX-S, Hayakawa Y, Toyama N, Matsuyama H, Iwamoto K, Suzuki H, Liu Y (2009) A study on subsurface structure model for deep sedimentary layers of Japan for strong-motion evaluation. Technical Note of the National Research Institute for Earth Science and Disaster Prevention 337:260

Gardner GHF, Gardner LW, Gregory AR (1974) Formation velocity and density—the diagnostic basics for stratigraphic traps. Geophysics 39:770–780. doi:10.1190/1.1440465

Gassenmeier M, Sens-Schönfelder C, Eulenfeld T, Bartsch M, Victor P, Tilmann F, Korn M (2016) Field observations of seismic velocity changes caused by shaking-induced damage and healing due to mesoscopic nonlinearity. Geophys J Int 204(3):1490–1502. doi:10.1093/gji/ggv529

Goldstein P, Snoke A (2005) SAC availability for the IRIS community, Incorporated Institutions for Seismology Data Management Center Electronic Newsletter. http://ds.iris.edu/ds/newsletter/vol7/no1/sac-availability-for-the-iris-community/

Hadziioannou C, Larose E, Coutant O, Roux P, Campillo M (2009) Stability of monitoring weak changes in multiply scattering media with ambient noise correlation: laboratory experiments. J Acoust Soc Am 125(6):3688–3695

Hobiger M, Wegler U, Shiomi K, Nakahara H (2012) Coseismic and postseismic elastic wave velocity variations caused by the 2008 Iwate-Miyagi Nairiku earthquake, Japan. J Geophys Res 117:B09313. doi:10.1029/2012JB009402

Holliger K, Levander AR (1992) A stochastic view of lower crustal fabric based on evidence from the Ivrea zone. Geophys Res Lett 19(11):1153–1156

Kanu C, Snieder R (2015) Time-lapse imaging of a localized weak change with multiply scattered waves using numerical-based sensitivity kernel. J Geophys Res Solid Earth 120(8):5595–5605

Maeda T, Obara K, Yukutake Y (2010) Seismic velocity decrease and recovery related to earthquake swarms in a geothermal area. Earth Planets Space 62:685–691. doi:10.5047/eps.2010.08.006

Matsubara M, Obara K (2011) The 2011 off the Pacific coast of Tohoku Earthquake related to a strong velocity gradient with the Pacific plate. Earth Planets Space 63(7):663–667

Meier U, Shapiro NM, Brenguier F (2010) Detecting seasonal variations in seismic velocities within Los Angeles basin from correlations of ambient seismic noise. Geophys J Int 181(2):985–996
Murnaghan FD (1967) Finite deformation of an elastic solid. Dover, New York, p. 124
Nakata N, Snieder R (2012) Time-lapse change in anisotropy in Japan's near surface after the 2011 Tohoku-Oki earthquake. Geophys Res Lett 39:L11313
Obermann A, Planès T, Larose E, Sens-Schönfelder C, Campillo M (2013a) Depth sensitivity of seismic coda waves to velocity perturbations in an elastic heterogeneous medium. Geophys J Int 194(1):72–382. doi:10.1093/gji/ggt043
Obermann A, Planès T, Larose E, Campillo M (2013b) Imaging preeruptive and coeruptive structural and mechanical changes of a volcano with ambient seismic noise. J Geophys Res: Solid Earth 118(12):6285–6294
Okada Y (1992) Internal deformation due to shear and tensile faults in a half-space. Bull Seism Soc Am 82(2):1018–1040
Okada Y, Kasahara K, Hori S, Obara K, Sekiguchi S, Fujiwara H, Yamamoto A (2004) Recent progress of seismic observation networks in Japan—Hi-net, F-net, K-net and KiK-net—. Earth Planets Space 56:15–28
Pacheco C, Snieder R (2005) Time-lapse travel time change of multiply scattered acoustic waves. J Acoust Soc Am 118(3):1300–1310
Pacheco C, Snieder R (2006) Time-lapse traveltime change of singly scattered acoustic waves. Geophys J Int 165(2):485–500
Poupinet G, Ellsworth WL, Frechet J (1984) Monitoring velocity variations in the crust using earthquake doublets: an application to the Calaveras fault, California. J Geophys Res 89:5719–5731. doi:10.1029/JB089iB07p05719
Prioul R, Bakulin A, Bakulin V (2004) Nonlinear rock physics model for estimation of 3D subsurface stress in anisotropic formations: theory and laboratory verification. Geophysics 69(2):415–425
Rivet D, Campillo M, Shapiro NM, Cruz-Atienza V, Radiguet M, Cotte N, Kostoglodov V (2011) Seismic evidence of nonlinear crustal deformation during a large slow slip event in Mexico. Geophys Res Lett 38:L08308. doi:10.1029/2011GL047151
Rubinstein JL, Beroza GC (2004) Nonlinear strong ground motion in the M_L 5.4 Chittenden earthquake: evidence that preexisting damage increases susceptibility to further damage. Geophys Res Lett 31:L23614
Rubinstein JL, Beroza GC (2005) Depth constraints on nonlinear strong ground motion from the 2004 Parkfield earthquake. Geophys Res Lett 32:L14313. doi:10.1029/2005GL023189
Sánchez-Sesma FJ, Campillo M (2006) Retrieval of the Green's function from cross correlation: the canonical elastic problem. Bull Seismol Soc Am 96(3):1182–1191
Sato H, Fehler MC, Maeda T (2012) Seismic wave propagation and scattering in the heterogeneous Earth. Springer, Berlin Heidelberg
Sawazaki K, Sato H, Nishimura T, Nakahara H (2009) Time-lapse changes of seismic velocity in the shallow ground caused by strong ground motion shock of the 2000 Western-Tottori earthquake, Japan, as revealed from coda deconvolution analysis. Bull Seismol Soc Am 99:352–366
Sawazaki K, Kimura H, Shiomi K, Uchida N, Takagi R, Snieder R (2015) Depth-dependence of seismic velocity change associated with the 2011 Tohoku earthquake, Japan, revealed from repeating earthquake analysis and finite-difference wave propagation simulation. Geophys J Int 201(2):741–763
Sens-Schönfelder C, Wegler U (2006) Passive image interferometry and seasonal variations of seismic velocities at Merapi Volcano, Indonesia. Geophys Res Lett 33:L21302. doi:10.1029/2006GL027797
Snieder R (2006) The theory of coda wave interferometry. Pure Appl Geophys 163(2-3):455–473
Snieder R, Şafak E (2006) Extracting the building response using seismic interferometry: theory and application to the Millikan Library in Pasadena, California. Bull Seism Soc Am 96(2):586–598
Takagi R, Okada T, Nakahara H, Umino N, Hasegawa A (2012) Coseismic velocity change in and around the focal region of the 2008 Iwate-Miyagi Nairiku earthquake. J Geophys Res 117:B06315. doi:10.1029/2012GL051342
TenCate JA, Smith E, Guyer RA (2000) Universal slow dynamics in granular solids. Phys Rev Lett 85(5):1020–1023
Ueno T, Saito T, Shiomi K, Enescu B, Hirose H, Obara K (2012) Fractional seismic velocity change related to magma intrusions during earthquake swarms in the eastern Izu peninsula, central Japan. J Geophys Res 117:B12305
Ueno T, Saito T, Shiomi K, Haryu Y (2015) Monitoring the instrument response of the high-sensitivity seismograph network in Japan (Hi-net): effects of response changes on seismic interferometry analysis. Earth Planets Space 67(1):1–10
Weaver RL, Hadziioannou C, Larose E, Campillo M (2011) On the precision of noise correlation interferometry. Geophys J Int 185(3):1384–1392
Wegler U, Sens-Schönfelder C (2007) Fault zone monitoring with passive image interferometry. Geophys J Int 168(3):1029–1033. doi:10.1111/j.1365-246X.2006.03284.x
Wessel P, Smith WHF, Scharroo R, Luis JF, Wobbe F (2013) Generic Mapping Tools: improved version released, EOS Trans. AGU 94:409–410
Yang W, Ge H, Wang B, Hu J, Yuan S, Qiao S (2014) Active source monitoring at the Wenchuan fault zone: coseismic velocity change associated with aftershock event and its implication. Earthq Sci 27(6):599–606. doi:10.1007/s11589-014-0101-0
Yarai H, Yamada S, Morishita Y, Kobayashi T, Tobita M (2015) Postseismic deformation of the 2014 Northern Nagano Prefecture Earthquake. 2015 Seism Soc Japan Fall Meeting S03:P15